# Densification study of Pr6O11 as a limiting step for the determination of its oxygen transport properties

Laura Guesnet, Élise Bonnet, Jean-Marc Heintz, E Chadourne, Jean-Claude Grenier, Thierry Chartier, Pierre -Marie Geffroy, Jean-Marc. Bassat

# Densification study of $Pr_6O_{11}$ as a limiting step for the determination of its oxygen transport properties

**L. Guesnet[1,2], E. Bonnet[1.2], J.M. Heintz[1], E. Chadourne[1], J.C. Grenier[1], T. Chartier[2], P.M. Geffroy[2] and J.M. Bassat[1,*]**

[1] *CNRS, Univ. Bordeaux, Bordeaux INP, ICMCB, UMR 5026, F-33600 PESSAC Cedex, France*

[2] *CNRS, Institut de Recherche sur les Céramiques (IRCER), UMR 7315, Centre Européen de la Céramique, 12 rue Atlantis, 87068 LIMOGES Cedex, France*

*Corresponding author. Tel: +33(5)40002753; fax: +33(5)40002761; *e-mail address:* jean-marc.bassat@icmcb.cnrs.fr

## Abstract

This study describes the successful sintering of $Pr_6O_{11}$, which is recently developed as a promising oxygen electrode for Solid Oxide Cells (SOCs). Using dense pellets or thin films is mandatory prior to an accurate measurement of the ionic transport properties *via* the isotopic oxyen exchange method here involved. Dilatometry experiments performed under different atmospheres (argon, air, oxygen) and sintering tests with different thermal cycles allowed overcoming the detrimental phase changes of $Pr_6O_{11}$ and densifying this oxide with a sintered relative density of 95%. Dense pellets of large sizes were prepared. In a second part, the ionic transport properties of $Pr_6O_{11}$ have been determined in the range 400 < T°C < 800 thanks to Isotopic Exchange Depth Profiling (IEDP) measurements.

**Key words: SOC oxygen electrode, sintering, $Pr_6O_{11}$, ionic conductivity**

## 1. Introduction

For the commercialization of SOCs (Solid Oxide Cells), the ceramic cells should have an improved lifetime and chemical stability, as well as a lower cost. An efficient way to achieve these objectives is to decrease their operating temperature, down to approximately 600°C [1]. However, at this reduced temperature, the electro-catalytic activity of air and fuel electrodes has to be improved. To optimize the performance of the cell when it operates in such a range of temperatures, the thickness of the electrolyte has to be reduced, and the surface can be modified *via* catalytic activation. It is also beneficial to increase the active surface area. One of the ways is to elaborate a composite electrode (containing both ionic and electronic conductors). In this case, the active reaction zones are only located at the junction between electronic and electrolyte conductors, which is especially detrimental regarding the efficiency of the oxygen electrode. The next step was then, in this latter case, to increase further the oxygen surface exchange kinetics by using a MIEC (mixed ion-electron conductor) electrode, then to delocalize the reaction(s) on the entire surface of the MIEC in the oxygen electrode [2-4].

Research breakthroughs have been achieved to improve the performance of cells, either by developing new materials or improving the microstructure of the electrodes. Regarding the second way, infiltration of a catalyst into a porous anionic conducting skeleton (for instance gadolinium-doped ceria, GDC) is a very interesting method to shape the SOCs oxygen electrodes and to improve their electrochemical performances. Infiltration has been widely used to fabricate novel architectured oxygen electrode structures based on LSM [5, 6], LSCF [7, 8], LSBT [9, 10] and Ruddlesden-Popper materials such as $La_{n+1}Ni_nO_{3n+1}$ (n= 1, 2, 3)-YSZ [11, 12] or $Nd_2NiO_{4+\delta}$ [13, 14]. These studies showed that the infiltrated electrodes provided superior performance compared to the conventionally sintered electrodes. It not only improves the catalytic activity (through the presence of dispersed nano-particles), but it also increases the ionic and electronic conductivity (through an interconnected network of nano-particles), which overall leads to an increase of TPB length and reduction of the cell resistance. A new composite oxide was developed at ICMCB in Bordeaux, a few years ago: the praseodymium oxide, $Pr_6O_{11}$, infiltrated in a Gd- doped ceria (GDC) backbone. This composite electrode allowed obtaining a very low polarization resistance ($R_p$ = 0,03 Ω·cm² at 600°C) [15]. Actually, thanks to the Pr+III/Pr+IV mixed valence, $PrO_x$ exhibits a good activity to reduce oxygen [16]. Following this result, several works aimed to prepare efficient electrodes where $Pr_6O_{11}$ was infiltrated as part of a composite oxygen electrode [see for instance refs 17 - 20].

Therefore, the characterization of the ionic conductivity of $Pr_6O_{11}$, which is currently not well-known, is of first importance for a better understanding of its efficient behavior as oxygen electrode. However, since this oxide is a mixed conductor, it is not possible to carry out conventional impedance measurements without the use of blocking electrodes. An alternative route is to perform Isotopic Exchange Depth Profiling (IEDP) measurements, or Electronic Conductivity Relaxation measurements (ECR) to determine the oxygen diffusion and surface exchange coefficients. In both cases it is absolutely mandatory to use dense pellets. However, upon heating, $Pr_6O_{11}$ easily changes to $Pr_9O_{16}$, $Pr_7O_{12}$ and/or $Pr_2O_3$, also depending on the surrounding $pO_2$ [21]. It is then highly challenging to obtain near fully dense materials without cracking with the right oxygen stoichiometry. To the best of our knowledge, no work about the optimization of an adapted thermal cycle for the full densification of $Pr_6O_{11}$ pellets has been already reported in the literature. This is the objective of the study reported in this article. In a first section, the optimization of the sintering process of $Pr_6O_{11}$ is described with regard to its behavior during thermal treatment under different atmospheres and for different thermal cycles (heating/cooling rates, dwells duration). In a second part, the ionic transport properties (D* and k* coefficients) of $Pr_6O_{11}$ sintered pellets have been determined by IEDP.

## 2. Experimental

The $Pr_6O_{11}$ powder under study was a commercial powder provided by Solvay company. The mean particle size of the initial powder was d50 = 5 µm because of agglomerates. Then, this powder was attrition milled in ethanol medium with zirconia balls (diameter of 2 mm) at 700 rpm during one hour. The final powder was poly-dispersed, with three mean particle sizes, located around $d_{50}$ = 200 nm, 600 nm and 2 µm, as determined by laser granulometry measurements in water.

To study $Pr_6O_{11}$ sintering, the powders were uniaxially pressed at 100 MPa or 200 MPa to prepare green pellets with a diameter of 6 mm: for the highest sintering temperature (1450°C) the applied pressure was 100 MPa while it was increased up to 200 MPa for lower sintering temperatures (see Table 1). Green relative densities were about 48 % $d_{th}$ (theoretical density) when pressed at 100 MPa and about 52 % $d_{th}$ for 200 MPa. According to our own XRD measurements the crystallographic structure of $Pr_6O_{11}$ was refined in the fluorite-type structure and then the corresonding theoretical density is 6.91 $g.cm^{-3}$. These pellets were then sintered using different sintering cycles, as described in the Results and Discussion part (Table 1), the goal being to densify the pellets to more than 95 % of relative density. Final densities were determined from the average value issued from geometrical measurements and from the Archimedes' method.

A second type of samples was prepared for the IEDP measurements (part 2.3). For this purpose, our goal was to sinter a unique pellet with a diameter of 25 mm, in order to polish it, then to cut it with a diamond saw to get small identical pieces to perform the different isotopic exchanges. The green pellets were prepared by uniaxial pressing at 200 MPa and sintered with the best sintering cycle.

## 2.1 Dilatometry measurements

Dilatometry measurements were performed using a horizontal dilatometer (Netzsch DIL 402 C) on cylindrical pellets with initial thickness of about 5 mm ($l_o$) (heating and cooling rates =5°C/min, dwell time = 10 min). The temperature ranged from room temperature up to 1450°C. Different atmospheres were used for the dilatometry measurements: Ar, air or $O_2$ and the gas flow was fixed to 75 ml/min.

## 2.2 Sintering cycles

Following the dilatometry measurements, two different thermal cycles were used, while maintaining the same heating and cooling rates at 5°C/min. In the first cycle, called “one-step sintering” the sintering temperature, surrounding atmosphere and dwell time were the adjustable parameters. The second cycle was the so-called “two step sintering”. This process is based on a first heating step performed at high temperature in order to induce the densification process, followed by a fast cooling, down to an intermediate temperature to continue the densification without grain growth. This procedure, described elsewhere, should lead to fine and dense microstructures [22-23].

## 2.3 IEDP measurements

The oxygen diffusion coefficient $D^*$ and surface exchange coefficient $k^*$ were determined by the so-called isotopic exchange depth profile (IEDP) technique combining isotopic exchange of $^{18}O$ (used as an oxygen tracer) and determination of the $^{18}O$ penetration profiles by TOF-SIMS (Time-Of-Flight Secondary Ion Mass Spectrometry) analyses. The procedure is described in detail elsewhere [24-26]. The ceramics were first abraded with silicon carbide papers of successive grades, and then polished with an alumina paste down to a roughness close to 0.3 µm. Prior to each exchange, a pre-annealing step was performed, which consisted of equilibrating the sample at the temperature of interest (same temperature as the subsequent exchange) in dry natural $^{16}O$ oxygen (99.9 % purity

with natural abundances for (all) the oxygen isotopes) at 210 mbar. The time used for the pre-anneal step in natural oxygen was always much longer (at least ten times) than the exchange time. In a second step the samples were annealed at a pressure of 210 mbar in an $^{18}O$ enriched atmosphere (97%, Eurisotop) for 400 < *T* °C < 800. In order to limit the oxygen stoichiometry change during the heating and cooling ramps, a tubular furnace was rapidly withdrawn to set the samples to the annealing temperature and later rolled off to rapidly cool it down. The $^{18}O$ penetration profiles, *i.e* normalized $^{18}O$ isotopic fraction ($^{18}O$ / ($^{16}O$ + $^{18}O$)), were recorded as a function of the analyzed depth using a TOF-SIMS 5 Ion-Tof SIMS apparatus with a $Cs^+$ ions source. From the $^{16}O^-$ and $^{18}O^-$ SIMS intensity data acquired, the normalized $^{18}O$ isotopic fraction was calculated. Due to the sintering issues related to this material (possible presence of cracks), several trials have been performed at a given temperature. The oxygen profiles were then fitted with an appropriate solution of the gas diffusion equation in solids, according to Fick's second law and given by Crank [27], *i.e.* relation (1):

$$C'(x) = \operatorname{erfc}\left(\frac{x\sqrt{D^*t}}{2}\right) - \exp\left(\frac{k}{D^*}x + \frac{k^2}{D^*}t\right)\operatorname{erfc}\left\{\left(\frac{x\sqrt{D^*t}}{2}\right) + \left(\frac{k}{D^*}\sqrt{D^*t}\right)\right\} \qquad (1)$$

with $\operatorname{erfc}(x) = \int_0^x \exp\left(-x^2\right)dx$ and $C'(x,t) = \frac{C(x,t) - C_0}{C_S - C_0}$

C(x,t) is the $^{18}O_2$ isotopic concentration in the solid obtained by SIMS at the depth x, C'(x,t) is the isotopic fraction corrected for the natural isotopic background level (referred to as $C_0$ = 0.2 %) and for the isotope enrichment of the gas (referred to as $C_s$ = 97%), t (s) is the duration of the isotope anneal; D* is the oxygen tracer diffusion coefficient and h = k* / D*, as previously defined.

## 3. Results and discussion

### 3.1 Sintering studies

The sintering behavior under air (dilatometric measurements) of a green $Pr_6O_{11}$ pellet, pressed at 100 MPa ($d_{green}$ = 48 % $d_{th}$) is presented in Fig. 1-a as a function of temperature. The derivative with respect to time of this curve, *i.e.* the shrinkage rate is given in Fig. 1-b (heating) and 1-c (cooling). A first small shrinkage is observed between 200 and 400°C, probably related to the departure of some volatile species (water, carbonates,…) and grain rearrangement [28]. The real densification begins above 700°C and an overall large shrinkage is observed, *i.e.* more than 20%, which seems

high according to the initial relative density of the green sample. Actually, many accidents are observed on the shrinkage curve. They are more clearly identified on the derivated curve. During heating (Fig. 1-b), a sharp discontinuity is observed between 1180 and 1220°C that will be refered in the following as $T_{discontinuity}$. This could be related to changes in the oxygen stoichiometry of $Pr_6O_{11}$ and therefore to crystallographic structure changes, as described in the literature [21, 29]. Previously reported TGA measurements showed that during heating under air, $Pr_6O_{11}$ is transformed into $Pr_9O_{16}$, $Pr_7O_{12}$ and/or $Pr_2O_3$ with an oxygen loss [21, 30]. A particular point concerns the cooling stage. A significant increase in linear shrinkage is also noticed below 1100°C: it corresponds to a large increase in the volume of the sample that is already densified and leading to macroscopic cracking of the ceramic. Correspondingly, a swelling of the sample is observed a few hours after the end of the cycle, resulting in a complete cracking of the pellet.

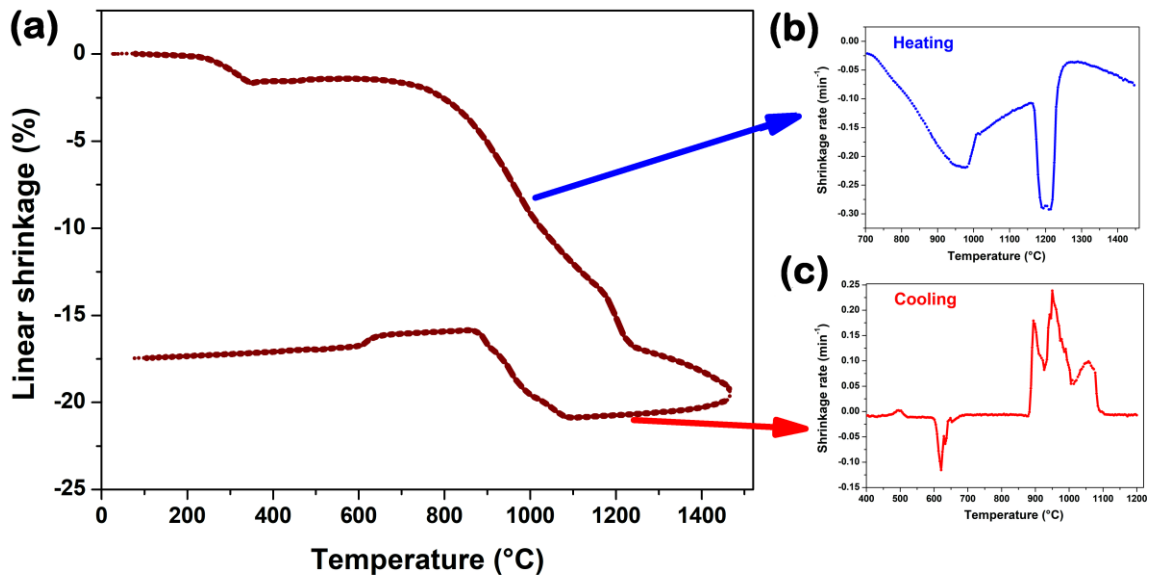


*Figure 1. Dilatometric behavior in air of a $Pr_6O_{11}$ green pellet ($d_{rel}$ = 59 % $d_{th}$) (a) linear shrinkage and (b) shrinkage rate (derivation of the curve 1-a with respect to the time) during (b) heating and (c) cooling as a function of temperature*

In order to avoid, or at least to limit these detrimental phenomena for getting high density and keeping the integrity of the material, likely correlated to the oxygen stoichiometry evolution of $Pr_6O_{11}$, densification experiments were carried out under different atmospheres (Fig 2). For the three selected oxygen partial pressures (*i.e.* 1, 0.2 and around 1 Pa for oxygen, air and argon, respectively), the initial behaviour remains the same, with a small initial shrinkage, while the densification only begins above 700°C. Then, the thermal behaviour of $Pr_6O_{11}$ samples strongly

depends on the sintering atmosphere. One can first notice the evolution of $T_{discontinuity}$ as a function of $Po_2$. It increases from Ar, to air and oxygen: $T_{discontinuity}$ ~ 1000°C, 1200°C and 1400°C respectively (see arrows in Fig. 2). This is in agreement with the transition temperature evolution of $Pr_6O_{11}$ towards $PrO_x$ compounds with higher oxygen content [21]. An opposite variation of dimension is observed during cooling. It occurs at the highest temperature under pure oxygen while no volume increase is observed under argon. For the latter case, after the dilatometric measurement, the pellet remains dense. However, one day later after staying at room temperature, it is swelled and turns partly yellow without keeping any mechanical cohesion. XRD analysis evidences a large amount of praseodymium hydroxide. Then, despite the absence of volume increase during cooling, the densification performed under argon atmosphere did not deserve our attention.

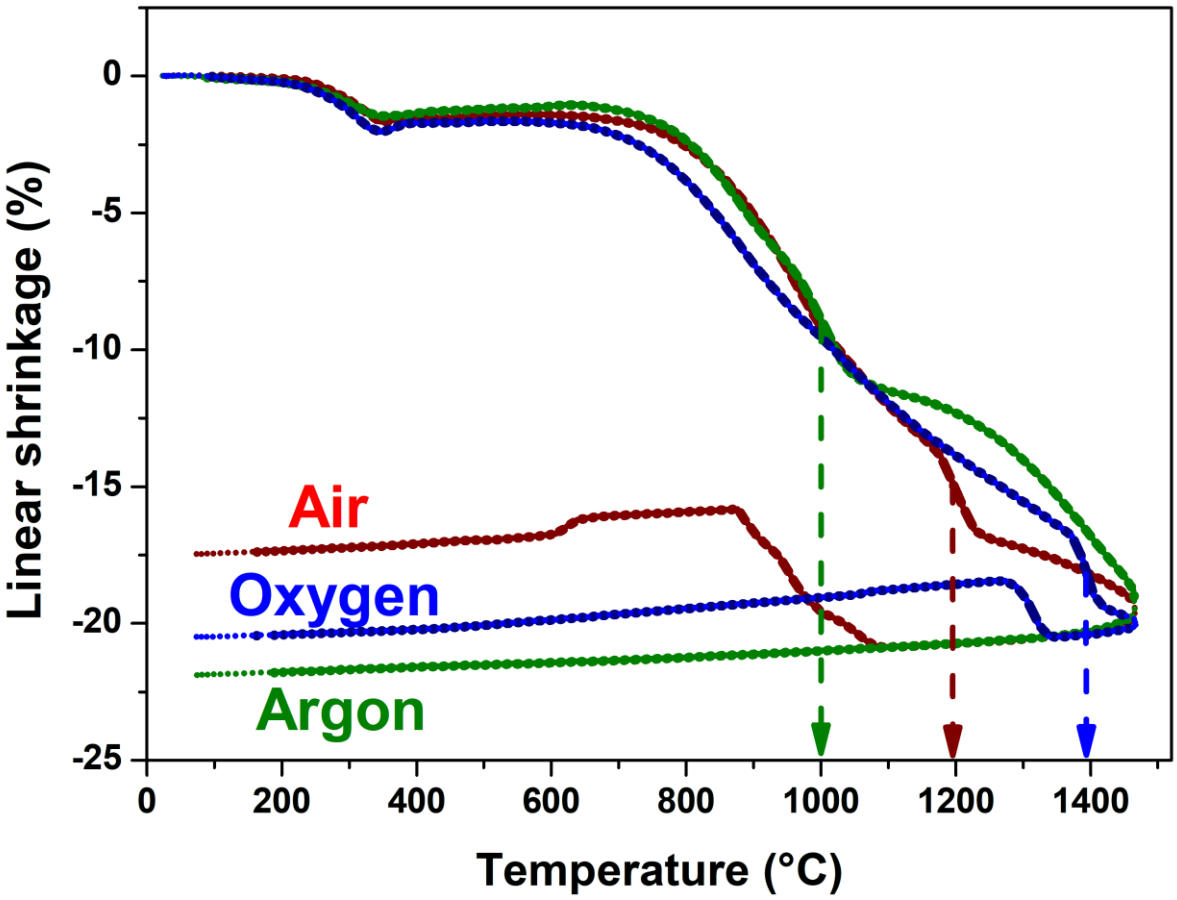


*Figure 2. Linear shrinkage of $Pr_6O_{11}$ green pellets heat-treated under argon, air or oxygen as a function of temperature (5°C/min heating and cooling rates).*

In the following, a more accurate study is then performed either under oxygen or under air, while keeping in mind that a thermal treatment performed under oxygen preferentially leads to the formation of $PrO_2$, which is a more oxidized phase than $Pr_6O_{11}$.

Regarding sintering under air, the large volume expansion observed below 1100°C should be avoided and then, two thermal cycles were considered. First, a long dwell time (30 h) was performed under air at 1100°C, in order to activate the sintering process before the phase transition (Table 1, cycle 1). Secondly, two-step sintering cycles were carried out: i) heating up to 1450°C, followed by a rapid cooling down to 1100°C (*i.e.* below the phase transition) with a plateau of 1 h (cycle 2); ii) heating up to 1150°C, followed by rapid cooling down to 1000°C, with a long dwell performed at this temperature (30 h, cycle 3). The objectives of the two-step sintering were to avoid the phase changes maintaining a high densification. Whatever the case, the relative density of the sintered pellets remained too low (81 % in the best case, cycle 2). Moreover, only one pellet did not break after thermal cycling, the one for which the transition temperature (1150°C) was not exceeded. Note that under argon no expansion is observed, giving strength to the hypothesis that the volume increase resulting in the crack of the pellet is directly related to an oxygen up-take.

Under oxygen, Fig. 2 shows that the pellet volume still increases during cooling, but to a lesser extend than under air. The final relative density in that case (1450°C with a dwell time of 10 min) is about 87 % (Table 1, cycle 4) and the ceramic appeared uncracked. An XRD analysis shows that $PrO_2$ is dominant, at least on the surface. A second thermal treatment was then performed at 700°C during 7 h under air to adjust the oxygen stoichiometry, which allowed recovering $Pr_6O_{11}$. Increasing the dwell time at 1450°C to 1 h (cycle 5) does not improve the relative density but increases the brittleness of the final ceramic. Actually, a simple sintering under oxygen did not allow obtaining dense and pure $Pr_6O_{11}$ ceramics.

Table 1 – Thermal cycles used for the sintering of $Pr_6O_{11}$ pellets (the diameter and thickness of the green pellets were 5 and 3 mm, respectively). The cold uniaxial pressure applied to prepare the green pellets was 100 MPa for the cycles 1 to 5, and 200 MPa for the cycles 6 to 10 (marked with a *). The lab co-precipitated powders were attrited (1h), and the resulting granulometry measurements evidences three populations, which are centered around 0.2, 0.6 and 1µm, respectively.

| **Thermal cycle** | **Dwell (T°/duration)** | **Visual observation** | **Sintered density ($g/cm^3$)** | **Relative density (%)** |
|---|---|---|---|---|
| **Air atmosphere – commercial powder** | | | | |
| 1 | 1100°C/30 h | Good | 5.4 | 78 |
| 2 | Two steps: 1450°C **+** 1100°C/1 h | Cracked pellet | 5.6 | 81 |
| 3 | Two steps: 1150°C **+** 1000°C/30 h | Cracked pellet after 1 week | 5.2 | 75 |

| | | | | |
|---|---|---|---|---|
| **Oxygen atmosphere – commercial powder** | | | | |
| 4 | 1450°C/0.16 h | Good | 6.0 | 87 |
| 5 | 1450°C/1 h | Some cracks | 6.0 | 87 |
| 6* | 1350°C/10 h | Good | 6.3 | 91 |
| 7* | 1370°C/15 h | Some cracks | 6.2 | 90 |
| 8* | 1355°C/40 h | Few cracks | 6.3 | 92 |
| **Oxygen atmosphere – lab co-precipitated powder** | | | | |
| 9* | 1355°C/40 h | Very few cracks | 6.4 | 93 |
| 10* | 1370°C/15 h + 700°C/7h under air | Good | 6,5 | **95** |

The analysis of the shrinkage curve under $O_2$ (Fig. 2) indicates that $T_{discontinuity}$ is around 1400°C, beginning at 1370°C, *i.e.* about 200°C higher than under air, which could be a favourable feature for improving the densification without crystallographic changes. So, the first attempts were made just below the phase transition temperature, *i.e.* 1370°C, by adjusting the sintering temperature and the dwell duration. It corresponded to cycles 6 to 9, reported in Table 1. Moreover, the uniaxial pressure applied to prepare the green pellets was increased from 100 to 200 MPa in order to improve the green relative density (from 48 to 52,5 % $d_{th}$) and therefore the final densities. These samples are marked with a star in Table 1. As a result, the sintered relative densities of sample 6 to 8 were increased up-to 92 %. However, some cracks remained after the thermal treatment performed at the highest temperature (1370°C) that should be too close to the phase transition temperature. A rather good result (92% of relative density) was obtained for T = 1355°C combined with a long duration dwell (40 h).

The last attempts were performed using a home-made powder that was prepared using a classical co-precipitation route, followed by an attrition step. Using that powder, a significant improvement in green density was obtained ($d_o$ = 57 % $d_{th}$), resulting in a final density ($d_f$ = 93 % $d_{th}$) slightly higher than the previous one, for the same sintering cycle at T = 1355°C during 40 h (cycle 9). Finally, a two stage sintering process was used involving two different atmospheres (cycle 10): 1) sintering at 1370°C during 15 h under oxygen; 2) cooling down to 700°C under air; 3) 7 h stage at 700°C in air (to fully recover the $Pr_6O_{11}$ phase), and then cooling under air down to room temperature (cycle 10). This last experiment gave the best sintered density, 95 % $d_{th}$, without any macroscopic cracks.

SEM observations of fractured sintered pellets obtained from cycles 5 and 10 are presented in Fig. 3. The respective relative densities are 87 % (Fig. 3-a) and 95 % (Fig.3-b). Fig. 3-a clearly evidences a quite high remaining porosity, with both closed and open porosity. Conversely, Fig. 3-b mostly shows spherical pores, characteristic of closed porosity. Image analysis (ImageJ software) of this

SEM micrograph gave a porosity of about 3 %, which is quite in agreement with the measured density. One could also notice the absence of visible cracks on this fractured sample.

As a conclusion, the cycle 10 allows obtaining dense and uncracked $Pr_6O_{11}$ ceramics. Therefore, this sintering treatment is selected to prepare large samples for the IEDP measurements as described in the following.

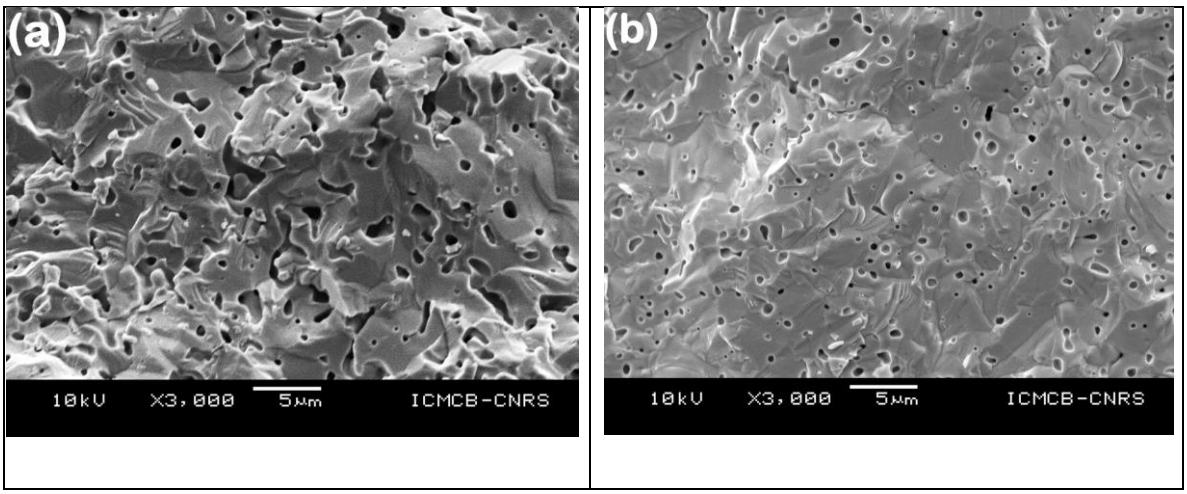


*Figure 3. SEM cross section micrographs of $Pr_6O_{11}$ pellets sintered (a) at 1450°C/1h under $O_2$ (cycle 5, $d_f$ = 87 % $d_{th}$), (b) at 1370°C/15 h under $O_2$ followed by a rapid cooling to 700°C under air with a 7 h stage (cycle 10, $d_f$ = 95 % $d_{th}$).*

3.2 Isotopic Exchange Depth Profiling (IEDP) measurements

A drawback encountered when using the previously sintered $Pr_6O_{11}$ pellets could be the presence of micro-cracks. It can be of course a major issue if the oxygen mapping is performed in such a kind of area, because the oxygen diffusion is accelerated in the crack compared to the bulk diffusion; it is well illustrated in Fig. 4a where an horizontal micro-crack is well visible causing an increase of the $^{18}O$ concentration (abnormally enhanced yellow part). This increase if larger and larger closer to the crack as oxygen can diffuse preferentially inside the crack. Such a feature would lead to an artificial increase of the isotopic oxygen concentration and then to an over-estimation of the D* and k* coefficients. On the contrary, Fig.4b which was obtained in a dense area without crack; a clear $^{18}O$ gradient (from yellow to red color, from the edge to the center of the pellet) was evidenced and used to determine the D* and k* coefficients.

Then, the mapping was carefully carried out in selected zones where the gradient remains constant along a significant thickness.

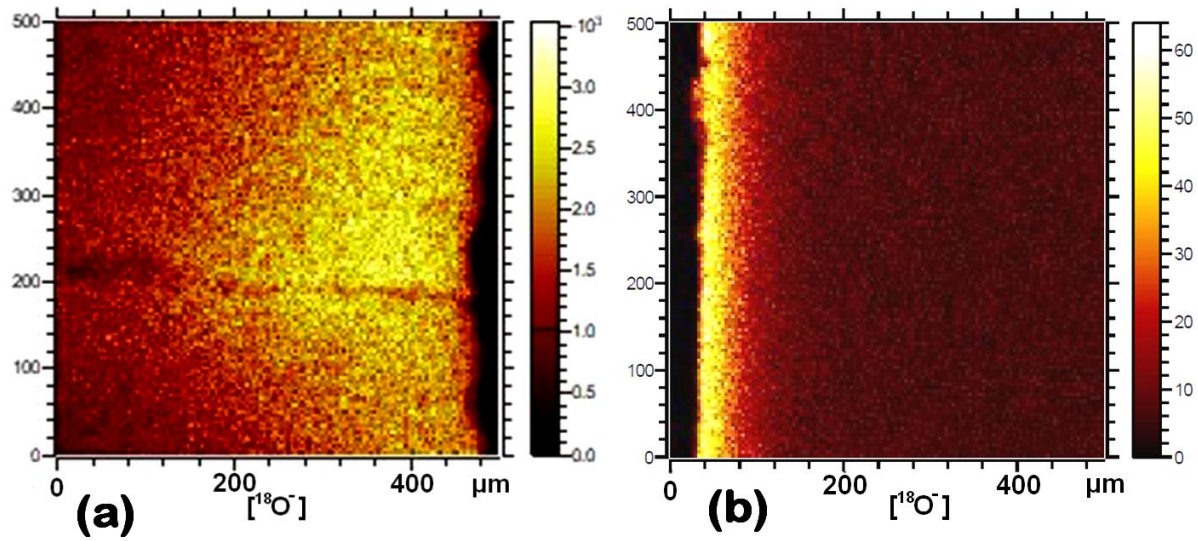


*Figure 4. a) Mapping of the $^{18}O$ concentration around a micro-crack area, observed after an oxygen isotopic exchange performed at T = 600°C during 4920s;*

*b) Mapping of the $^{18}O$ concentration in a dense area, without crack, observed after an oxygen isotopic exchange performed at T = 400°C during 15420s.*

IEDP measurements were performed in the range 400 – 800°C. An example of profile, *i.e.* the evolution of the normalized $^{18}O$ concentrations ($[^{18}O] / [^{18}O]+ [^{16}O]$) *vs.* pellet thickness is shown in Fig. 5 (T = 400°C, exchange duration time: 15420s).

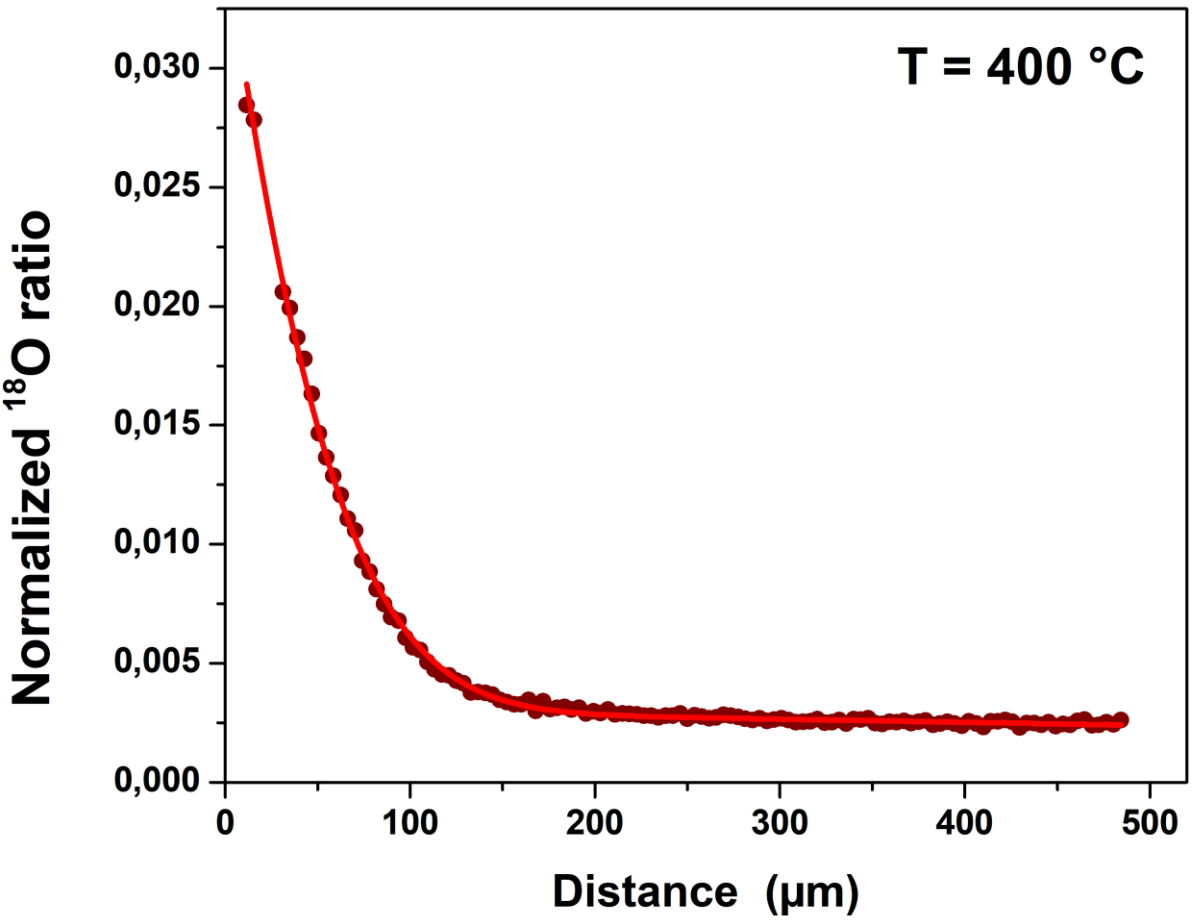


*Figure 5. $^{18}$O diffusion profile recorded by TOF-SIMS analysis on a $Pr_6O_{11}$ pellet after oxygen isotopic exchange performed at T = 400°C during 15420s.*

The initial (distance = 0 µm) normalized $^{18}$O ratio ($^{18}$O / $^{18}$O + $^{16}$O) is un-expectedly quite low (it was the case for each of the performed exchanges). However, the most important point is that the ratio in the "queue" of the profile, *i.e.* when no diffusion occurs, is very close to the natural abundancy of the $^{18}$O isotope, *i.e.* 0.2%. The analysis of the fit allows to accurately determine the D* and k* coefficients according to relation (1): D* = $1.73 \times 10^{-9} \pm 2.46 \times 10^{-11}$ cm$^2$.s$^{-1}$, k* = $1.02 \times 10^{-8} \pm 6.59 \times 10^{-11}$ cm.s$^{-1}$ at T = 400°C.

The temperature dependences of the D* and k* coefficients are plotted in Figs 6 and 7, respectively.

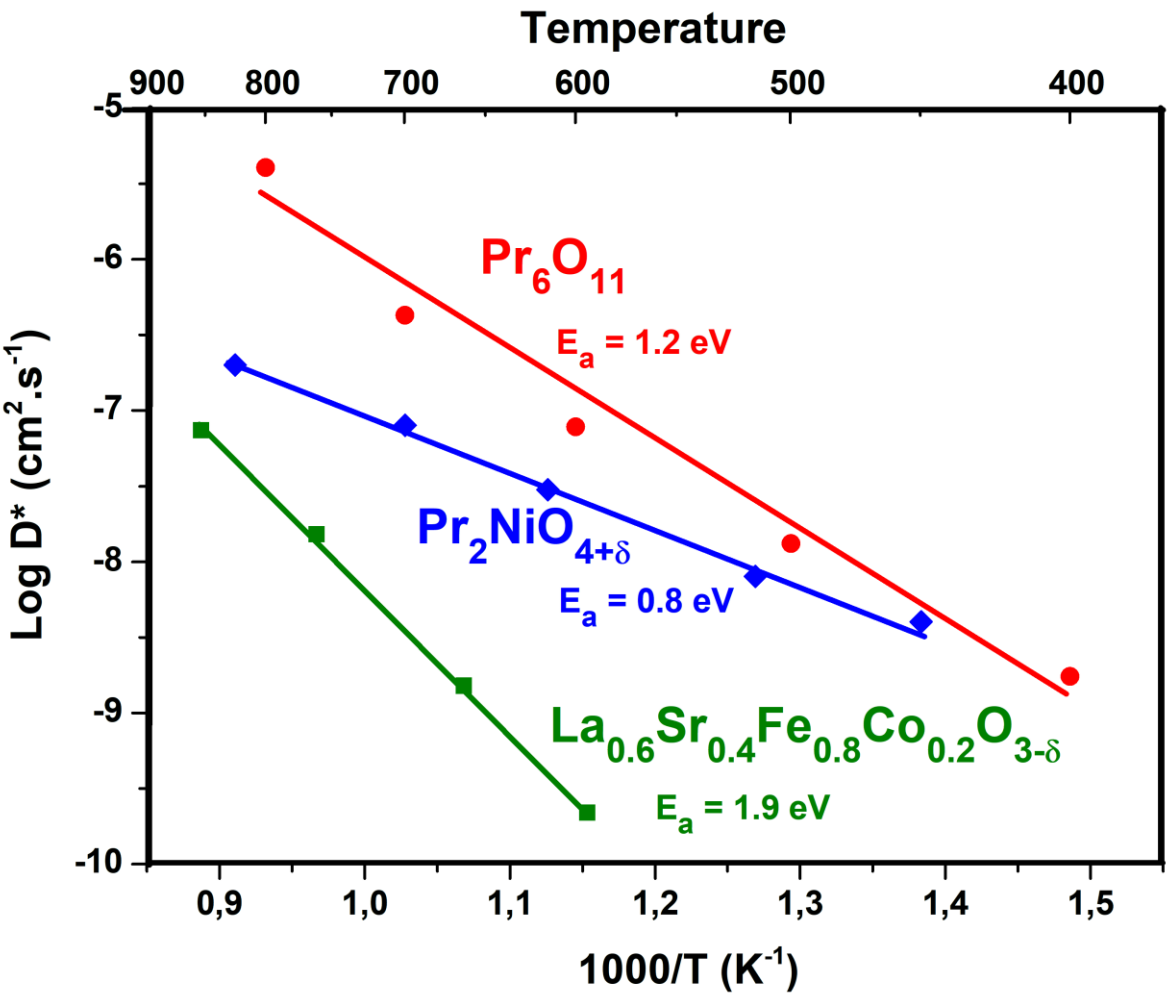


Figure 6. Arrhenius plot of the D* coefficient vs. 1000/T determined for $Pr_6O_{11}$. Comparison with the corresponding values determined for $Pr_2NiO_{4+\delta}$ [31], and $La_{0.6}Sr_{0.4}Fe_{0.8}Co_{0.2}O_{3-\delta}$ [32].

Fig. 6 clearly evidences that the oxygen diffusion coefficient of $Pr_6O_{11}$ is significantly higher than those of other usual oxygen electrode materials used for SOC applications, such as $Pr_2NiO_{4+\delta}$, and $La_{0.6}Sr_{0.4}Fe_{0.8}Co_{0.2}O_{3-\delta}$. Especially, the very high mobility of oxide ions in $Pr_6O_{11}$ observed at low temperature is likely one of the main reasons of the exceptional catalytic properties and electrochemical performances as oxygen electrode material at 600-400°C. Besides, the activation energy associated to oxygen transport mechanism for $Pr_6O_{11}$ is close to 1.2 eV (determined in the 450 < T°C < 800 temperature range), *i.e.* similar to the value observed for yttrium doped zirconia (1.1eV-0.97eV) [33].

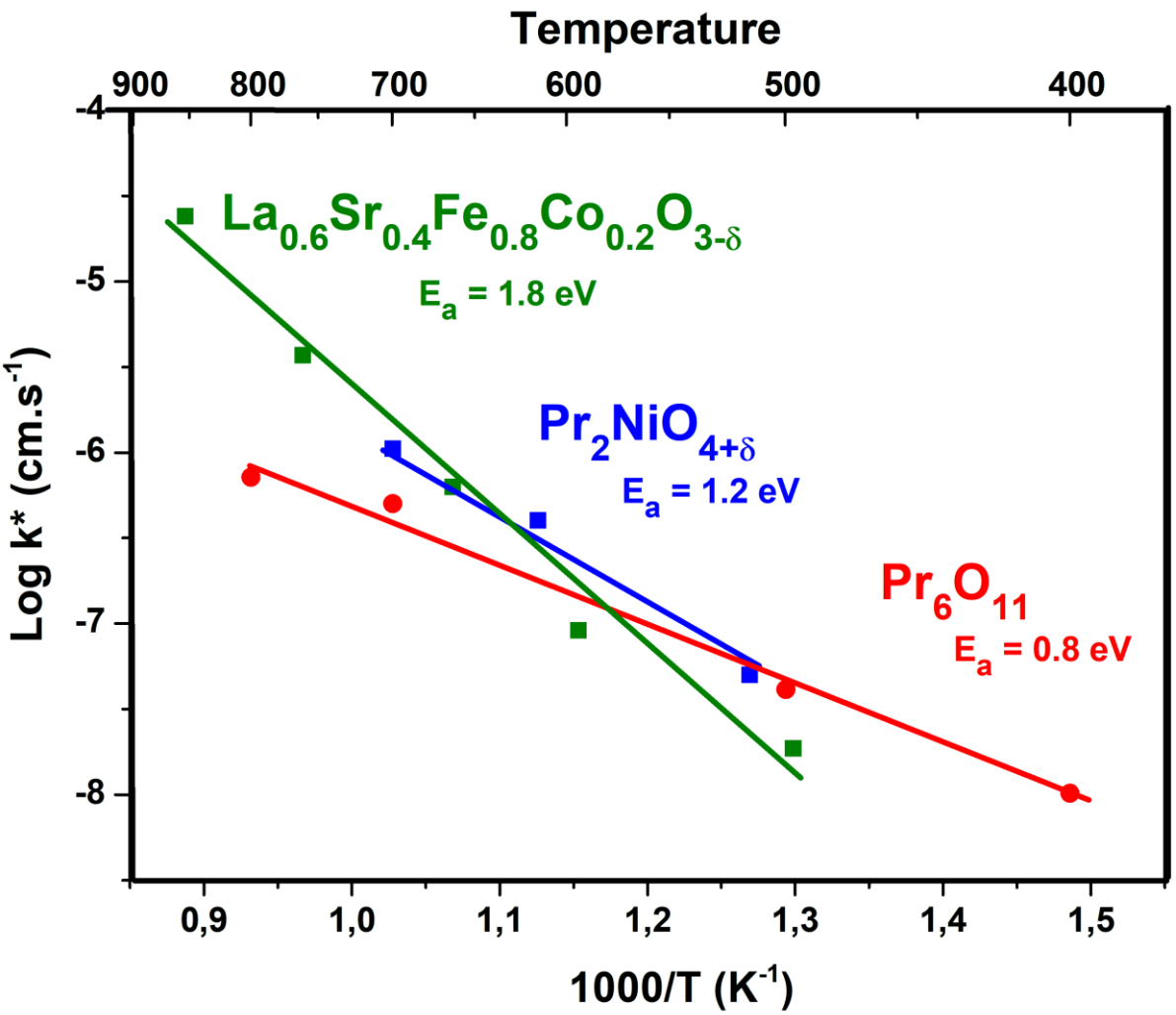


Figure 7. Arrhenius plot of the k* coefficient vs. 1000/T determined for $Pr_6O_{11}$. Comparison with the corresponding values determined for $Pr_2NiO_{4+\delta}$ [31], and $La_{0.6}Sr_{0.4}Fe_{0.8}Co_{0.2}O_{3-\delta}$ [32].

Fig. 7 evidences that the oxygen surface exchange coefficient for $Pr_6O_{11}$ is somewhat higher or at least comparable to those of other usual materials (*i.e.* $Pr_2NiO_{4+\delta}$ and $La_{0.6}Sr_{0.4}Fe_{0.8}Co_{0.2}O_{3-\delta}$) at low temperature (< 550°C). Besides, the activation energy associated to the oxygen surface exchange mechanism at the surface of $Pr_6O_{11}$ is exceptionally low (0.8eV, determined in the 400 < T°C < 800 temperature range), in comparison with those of $Pr_2NiO_{4+\delta}$ and $La_{0.6}Sr_{0.4}Fe_{0.8}Co_{0.2}O_{3-\delta}$, 1.2 eV and 1.8 eV, respectively.

De Souza evidenced a strong correlation between the D* and k* coefficients for numerous mixed ionic and electronic conductors (MIEC) [34]. For instance, MIEC materials with the highest oxygen diffusion coefficients (D*) also exhibit the highest oxygen exchange coefficient (k*). Then, the exceptional electrochemical performances of $Pr_6O_{11}$, in particular the high oxygen exchange

coefficient (k*), could be mainly linked to the high oxygen mobility (or D*) in $Pr_6O_{11}$ structure at low temperature (600-400°C).

The ionic conductivity ($\sigma_{ion}$) evolution *vs*. 1000/T was evaluated using the Nernst-Einstein relation (2),

$$\sigma_{ion} = -\frac{4F^2 C_O D_O}{RT} \qquad (2)$$

where the oxygen diffusion coefficient $D_O$ is assumed to be close to D*, the oxygen molar concentration ($C_O$) is equal to 0.073 mol.cm$^{-3}$ for $Pr_6O_{11}$ (the lattice parameter of $Pr_6O_{11}$ being a = 5.494 Å); R is the universal gas constant, F, the Faraday's constant and T, the temperature (K).

Fig. 8 shows the temperature dependence of the calculated ionic and measured total conductivities, and ionic transport *vs.* temperature for $Pr_6O_{11}$. The ionic transport number was determined using the following relation (3):

$$t_i = \frac{\sigma_{ion}}{\sigma_{Total}} \qquad (3)$$

As expected, in the temperature range 400-800°C, $Pr_6O_{11}$ is a mixed ionic and electronic conductor with predominant electronic conductivity at low temperature (which was measured in ref. [35]). For instance the calculated ionic transport number of $Pr_6O_{11}$ is close to 0.064 at 700°C and close to 0.022 at 600°C; it is particularly high in comparison with other MIEC materials; as a comparison the ionic transport number of $La_{0.6}Sr_{0.4}Fe_{0.8}Co_{0.2}O_{3-\delta}$ is smaller than $10^{-4}$ at 700°C, a value which was determined from the ionic and electronic conductivity values available in the literature [36].

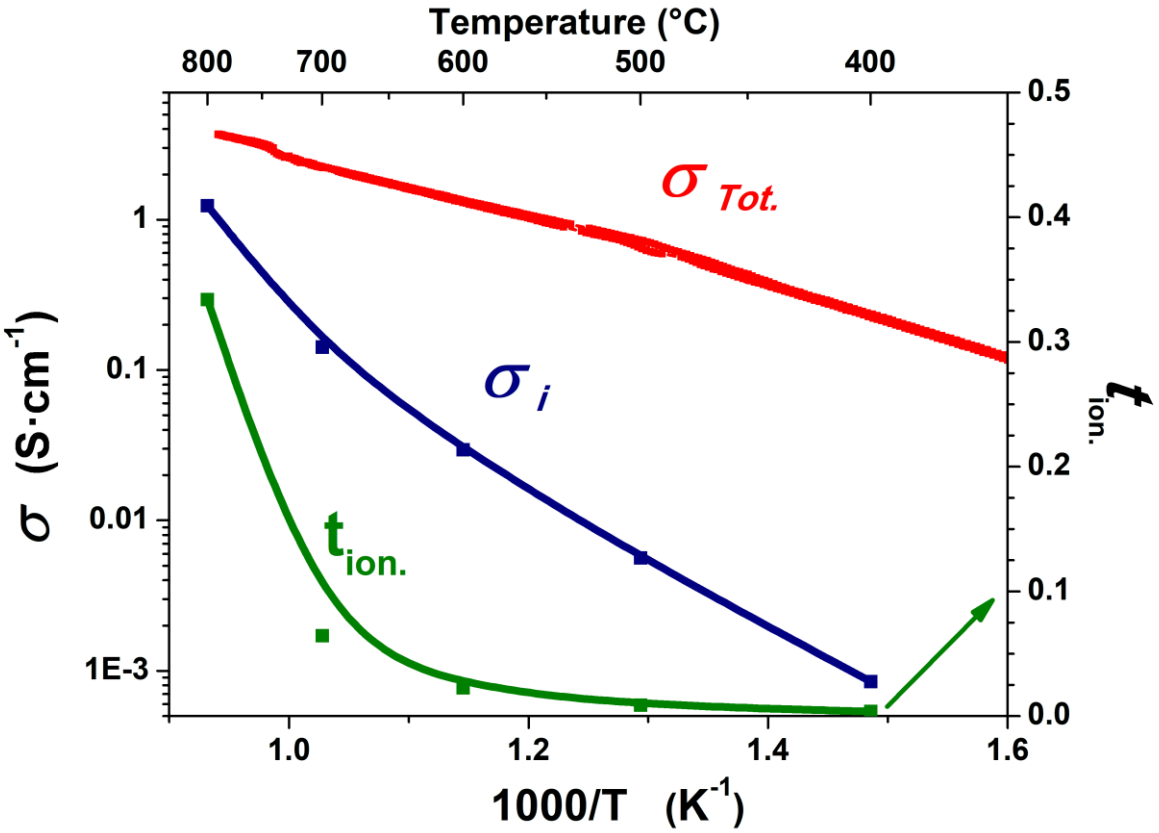


Figure 8. Temperature dependences of ionic [this work] and electronic conductivities [35] (left Y axis) and ionic transport number (right Y axis) for $Pr_6O_{11}$.

## Conclusions

$Pr_6O_{11}$ is a recently developed very efficient SOC oxygen electrode material which has been much studied during the last five years, mainly as a composite with gadolinium doped ceria (deposited using an infiltration way). This oxide can be expected to have good ion transport properties but, to our knowledge, no results published to date have confirmed this point. A reason could be the issues which are encountered when sintering the $Pr_6O_{11}$ pellets (in order to obtain a relative density ≥ 94%). It is indeed a limiting step prior to the determination of electronic and ionic transport properties, with respect to the easy formation of phases such as $Pr_9O_{16}$, $Pr_7O_{12}$ and / or $Pr_2O_3$, having different oxygen stoichiometries depending on the temperature and surrounding atmosphere. Indeed, such phase transitions induce dimensional variations which lead to the formation of cracks and possibly to the break of the pellet.

In this context, the sintering of a commercial $Pr_6O_{11}$ powder has been carefully studied, in particular by varying the thermal cycles and the nature of the atmosphere according to the various phase

transitions. The combination of two thermal cycles, a first one performed at high temperature (1370°C) under oxygen, followed by a second one at 700°C under air in order to recover the stoichiometry of oxygen led to dense $Pr_6O_{11}$ pellets with a relative density of 95%.

Then, D* and k* coefficients were determined in the temperature range 400 - 800°C. The results confirm that the oxygen mobility (*i.e.* the oxygen diffusion coefficient) is very high in the structure of $Pr_6O_{11}$ and especially at low temperature, significantly higher than the one of usual oxygen electrode materials, such as $Pr_2NiO_{4+\delta}$ or $La_{0.6}Sr_{0.4}Fe_{0.8}Co_{0.2}O_{3-\delta}$. Besides, the oxygen surface exchange coefficient is also higher than the ones of $Pr_2NiO_{4+\delta}$ and $La_{0.6}Sr_{0.4}Fe_{0.8}Co_{0.2}O_{3-\delta}$ at low temperatures, with a low activation energy, close to 0.7eV. The exceptional electrochemical performances of $Pr_6O_{11}$ as oxygen electrode materials for SOC applications is obviously linked to the oxygen transport properties of $Pr_6O_{11}$, showing high D* and k* coefficients at low temperature (600-400°C).

## References


[1] R. Knibbe, A. Hauch, J. Hjelm, S. D. Ebbesen, et M. Mogensen, « Durability of Solid Oxide Cells », *Green*, p. 141‑ 199, 2011.

[2] S. B. Adler, "Factors Governing Oxygen Reduction in Solid Oxide Fuel Cell Cathodes", *Chemical Reviews*, (104) (2004) 4791-4843.

[3] H. Yokokawa, H. Tu, B. Iwanschitz, A. Mai, *Journal of Power Sources*, 182 (2008) 400-412.

[4] G.C. Kostogloudis, C. Ftikos, *Solid State Ionics*, 126 (1999) 143-151.

[5] Sholklapper, Tal Z., Chun Lu, Craig P. Jacobson, Steven J. Visco, and Lutgard C. De Jonghe. 2006. LSM-Infiltrated Solid Oxide Fuel Cell Cathodes, *Electrochemical and Solid-State Letters*, 9: A376.

[6] Laguna-Bercero, M. A., A. R. Hanifi, T. H. Etsell, P. Sarkar, and V. M. Orera. 2015. Microtubular solid oxide fuel cells with lanthanum strontium manganite infiltrated cathodes, *International Journal of Hydrogen Energy*, 40: 5469-74.

[7] Shah, M., and S. A. Barnett. 2008. Solid oxide fuel cell cathodes by infiltration of La0.6Sr0.4Co0.2Fe0.8O3−δ into Gd-Doped Ceria, *Solid State Ionics*, 179: 2059-64.

[8] Burye, Theodore E., Hongjie Tang, and Jason D. Nicholas. 2016. The Effect of Precursor Solution Desiccation or Nano-Ceria Pre-Infiltration on Various La0.6Sr0.4FeyCo1-yO3-x Infiltrate Compositions, *Journal of The Electrochemical Society*, 163: F1017-F22.

[9] Vincent, Adrien L., Amir R. Hanifi, Jing-Li Luo, Karl T. Chuang, Alan R. Sanger, Thomas H. Etsell, and Partha Sarkar. 2012. Porous YSZ impregnated with La0.4Sr0.5Ba0.1TiO3 as a possible composite anode for SOFCs fueled with sour feeds, *Journal of Power Sources*, 215: 301-06.

[10] Vincent, Adrien L., Amir R. Hanifi, Mark Zazulak, Jing-Li Luo, Karl T. Chuang, Alan R. Sanger, Thomas Etsell, and Partha Sarkar. 2013. Preparation and characterization of an solid oxide fuel cell tubular cell for direct use with sour gas, *Journal of Power Sources*, 240: 411-16.

[11] Li, Ying, Shan-Lin Zhang, Cheng-Xin Li, Tao Wei, Guan-Jun Yang, Chang-Jiu Li, and Meilin Liu. 2016. La2NiO4+δ Infiltration of Plasma-Sprayed LSCF Coating for Cathode Performance Improvement, *Journal of Thermal Spray Technology*, 25: 392-400.

[12] Choi, Sihyuk, Seonyoung Yoo, Jee-Young Shin, and Guntae Kim. 2011. High Performance SOFC Cathode Prepared by Infiltration of Lan + 1NinO3n + 1 (n = 1, 2, and 3) in Porous YSZ, *Journal of The Electrochemical Society*, 158: B995.

[13] Laguna-Bercero, Miguel A., Amir R. Hanifi, Hernán Monzón, Joshua Cunningham, Thomas H. Etsell, and Partha Sarkar. 2014. High performance of microtubular solid oxide fuel cells using Nd2NiO4+δ-based composite cathodes, *Journal of Materials Chemistry A*, 2: 9764-70.

[14] Chen, Ting, Minquan Liu, Chun Yuan, Yucun Zhou, Xiaofeng Ye, Zhongliang Zhan, Changrong Xia, and Shaorong Wang. 2015. 'High performance of intermediate temperature solid oxide electrolysis cells using Nd2NiO4+δ impregnated scandia stabilized zirconia oxygen electrode', *Journal of Power Sources*, 276: 1-6.

[15] C. Nicollet, A. Flura, V. Vibhu, A. Rougier, J.M. Bassat and J.C. Grenier, “An innovative efficient oxygen electrode for SOFC: $Pr_6O_{11}$ infiltrated into Gd-doped ceria backbone” *International Journal of Hydrogen Energy,* (41) (34) (2016) 15538-15544.

[16] P. V. Hendriksen, M. Khoshkalam, X. Tong, D. Tripkovic, M. A. Faghihi-Sani, M. Chen, "Improving oxygen electrodes by infiltration and surface decoration", *The Electrochemical Society*, (91) (1) (2019) 1413-1424.

[17] Enhanced activity of PrO and CuO infiltrated Ce . Gd . O based composite oxygen electrodes By: Khoshkalam, Mohamad; Faghihi-Sani, Mohammad Ali; Tong, Xiaofeng; Chen, Ming; Hendriksen, Peter Vang, Journal of the Electrochemical Society (2020), 167(2), 024505

[18] Highly efficient architectured $PrO_x$ oxygen electrode for solid oxide fuel cell By: Sharma, Rakesh K.; Khamidy, Nur I.; Rapenne, Laetitia; Charlot, Frederic; Moussaoui, Hamza; Laurencin,Jerome; Djurado, Elisabeth, Journal of Power Sources (2019), 419, 171-180

[19] J. Garcia-Fayos, R. Ruhl, L. Navarrete, H. J. M. Bouwmeester, J. M. Serra, "Enhancing oxygen permeation through $Fe_2NiO_4$–$Ce_{0.8}Tb_{0.2}O_{2-\delta}$ composite membranes using porous layers activated with $Pr_6O_{11}$ nanoparticles", *Journal of Materials Chemistry A*, (6) (2018) 1201-1209.

[20] Y. Wang, T. Su, A. D. Brocato, X. D. Zhou, "Promotion of SOFC cathode performance and durability by the addition of mixed conducting praseodymium oxides", *The Electrochemical Society*, (91) (1) (2019), 1527-1533.

[21] B.G. Hyde, D.J.M. Bevan and L. Eyring, “on the praseodymium oxygen system” in “mathematical and physical sciences, vol 259, 1966, p.583-614.

[22] I.-Wei Chen & X.-H. Wang, Sintering dense nanocrystalline ceramics without final-stage grain growth, *Nature* (2000) 404, 168_171

[23] K. V. Mahesh, S. Anas, S. Rahul, et S. Ananthakumar, « Effect of two-step sintering on rare earth (RE = $Y_2O_3$, $Pr_6O_{11}$) doped ZnO–$Bi_2O_3$ varistors processed from ‘nano-precursor’ powders », *Journal of Materials Science*, vol. 24, p. 1495‑ 1504, 2013.

[24] R. A. De Souza, J. Zehnpfenning, M. Martin, J. Maier, "Determining oxygen isotope profiles in oxides with Time-of-Flight SIMS", *Solid State Ionics,* 176 (2005) 1465–1471.

[25] J.-M. Bassat, M. Petitjean, J. Fouletier, C. Lalanne, G. Caboche, F. Mauvy, J.-C. Grenier, "Oxygen isotopic exchange: A useful tool for characterizing oxygen conducting oxides", *Applied Catalysis A: General,* (289) (1) (2005) 84–89.

[26] R.J. Chater, S. Carter, J.A. Kilner, B.C.H. Steele, *Solid State Ionics*, (859) (1992) 53–56.

[27] J. Crank, "The Mathematics of Diffusion", Clarendon Press, Oxford, 2nd Edition, (1975).

[28] B. L. Treu, W. G. Fahrenholtz, and M. J. O'Keefe, Thermal Decomposition Behavior of Praseodymium Oxides, Hydroxides, and Carbonates, *Inorganic Materials*, 2011, Vol. 47, No. 9, pp. 974–978.

[29] F. J. Lincoln, J.R. Sellar and B.G. Hyde, A New Examination of the Thermodynamic Properties of the Oxygen-Deficient Fluorite-Type Phase $\alpha$-$PrO_{2-\delta}$, J. Solid State Chem, 74, 268_76 (1988).

[30] R. Turcotte, J. Warmkessel, R. Tilley and L. Eyring, Journal of Solid State Chemistry 3, 265 (1971).

[31] J.M. Bassat, M. Burriel, O. Wahyudi, R. Castaing, M. Ceretti, P. Veber, I. Weill, A. Villesuzanne, J.C. Grenier, W. Paulus, J. A. Kilner, Anisotropic Oxygen Diffusion Properties in $Pr_2NiO_{4+\delta}$ and $Nd_2NiO_{4+\delta}$ Single Crystals, *J. Phys. Chem. C 2013, 117, 26466−26472.*

[32] S. J. Benson, Oxygen Transport and Degradation Processes in Mixed Conducting Oxides, PhD thesis, Imperial College, 1999.

[33] R.A. De Souza, A universal empirical expression for isotope exchange coefficients (k*) of acceptor-doped perovskite and fluorite oxides, *Physical Chemistry Physics, 8 (2006) 890-897.*

[34] M. Filal, C. Petot, M. Mokchah, C. Chateau, J.L. Carpentier, Ionic conductivity of yttrium-doped zirconia and the "composite effect", Solid State Ionics 80 (1995) 27-35.

[35] C. Nicollet, « Nouvelles électrodes à oxygène pour SOFC à base de nickelates $Ln_2NiO_{4+\delta}$ (Ln = La, Pr) préparées par infiltration », PhD Thesis, University of Bordeaux, 2016.

[36] A. Mineshige, J. Izutsu, M. Nakamura, K. Nigaki, J. Abe, M. Kobune, S. Fujii and T. Yasawa, Introduction of A-side deficiency into $La_{0.6}Sr_{0.4}Co_{0.2}Fe_{0.8}O_{3-\delta}$ and its effect on structure and conductivity, Solid State Ionics 176 (2005), 1145-1149.

**Figure captions**

Fig. 1 *Dilatometric behavior in air of a $Pr_6O_{11}$ green pellet ($d_{rel}$ = 59 % $d_{th}$) (a) linear shrinkage and (b) sintering rate as a function of time and temperature (derivation of the curve 1-a with respect to the time) during (b) heating and (c) cooling as a function of temperature.*

Fig. 2 *Linear shrinkage of a $Pr_6O_{11}$ green pellet heat-treated under argon, air and oxygen as a function of temperature (5°C/min heating and cooling rate).*

Fig. 3 *SEM cross section micrographs of $Pr_6O_{11}$ pellets sintered :*
*(a) at 1450°C/1h under $O_2$ (cycle 5, $d_f$ = 87 % $d_{th}$),*
*(b) at 1370°C/15 h under $O_2$ followed by a rapid cooling to 700°C under air with a 7 h stage (cycle 10, $d_f$ = 95 % $d_{th}$).*

Fig. 4 *a) Mapping of the $^{18}O$ concentration around a micro-crack area, observed after an oxygen isotopic exchange performed at T = 600°C during 4920s; b) Mapping of the $^{18}O$ concentration in a dense area, without crack, observed after an oxygen isotopic exchange performed at T = 400°C during 15420 s.*

Fig. 5 *$^{18}O$ diffusion profile recorded by TOF-SIMS analysis on a $Pr_6O_{11}$ pellet after oxygen isotopic exchange performed at T = 400°C during 15420 s.*

Fig. 6 *Arrhenius plot of the D* coefficient vs. 1/T determined for $Pr_6O_{11}$. Comparison with the corresponding values determined for $Pr_2NiO_{4+\delta}$ [31], and $La_{0.6}Sr_{0.4}Fe_{0.8}Co_{0.2}O_{3-\delta}$ [32].*

Fig. 7 *Arrhenius plot of the k* coefficient vs. 1000/T determined for $Pr_6O_{11}$. Comparison with the corresponding values determined for $Pr_2NiO_{4+\delta}$ [31], and $La_{0.6}Sr_{0.4}Fe_{0.8}Co_{0.2}O_{3-\delta}$ [32].*

Fig. 8 *Temperature dependences of ionic [this work] and electronic conductivities [35] (left Y axis) and ionic transport number (right Y axis) for $Pr_6O_{11}$.*